

Unexpected Electron Transport Suppression in a Heterostructured Graphene-MoS₂ Multiple Field-Effect Transistor Architecture

Gaia Ciampalini,^{*,†,‡,¶} Filippo Fabbri,[¶] Guido Menichetti,^{‡,†} Luca Buoni,[†] Simona Pace,^{‡,§} Vaidotas Mišeikis,^{‡,§} Alessandro Pitanti,[¶] Dario Pisignano,^{†,¶} Camilla Coletti,^{‡,§} Alessandro Tredicucci,^{†,¶} and Stefano Roddaro^{†,¶}

[†]*Dipartimento di Fisica “E. Fermi,” Università di Pisa, Largo B. Pontecorvo 3, I-56127 Pisa, Italy*

[‡]*Graphene Labs, Istituto Italiano di Tecnologia, Via Morego 30, I-16163 Genova, Italy*
[¶]*NEST, CNR—Istituto Nanoscienze and Scuola Normale Superiore, piazza San Silvestro 12, I-56127 Pisa, Italy*

[§]*Center for Nanotechnology Innovation @NEST, Istituto Italiano di Tecnologia, Piazza San Silvestro 12, I-56127 Pisa, Italy*

E-mail: gaia.ciampalini@phd.unipi.it

Abstract

We demonstrate a graphene-MoS₂ architecture integrating multiple field-effect transistors (FETs) and we independently probe and correlate the conducting properties of van der Waals coupled graphene-MoS₂ contacts with the ones of the MoS₂ channels. Devices are fabricated starting from high-quality single-crystal monolayers grown by chemical vapor deposition. The heterojunction was investigated by scanning Raman and photoluminescence spectroscopies. Moreover, transconductance curves of MoS₂ are compared with the current-voltage characteristics of graphene contact stripes, revealing a significant suppression of transport on the *n*-side of the transconductance curve. Based on *ab Initio* modeling, the effect is understood in terms of trapping by sulfur vacancies, which counter-intuitively depends on the field-effect, even though the graphene contact layer is positioned between the backgate and the MoS₂ channel.

Keywords

graphene, MoS₂, heterostructure, field-effect, single-crystal

Van der Waals (vdW) heterostructures, formed when two or more atomically-thin crystals are bonded by vdW interaction,¹ are intriguing architectures, enabled by the discovery of two-dimensional (2D) materials, such as graphene, hexagonal boron nitride, and transition metal dichalcogenides (TMDs). Within this family, peculiar junctions can be obtained when graphene is used as a contact material for a TMD monolayer. While the interface between a TMD and a conventional, bulk metallic electrode tends to display Schottky behavior due to intrinsic and extrinsic Fermi pinning phenomena,^{2–4} vdW graphene-TMD junctions yield well-behaved linear transport characteristics.⁵ This contacting approach has been successful in improving TMD-based devices⁶

and, together with the side-contacting approach,^{7–9} is commonly used for the realization of most devices based on two-dimensional materials. Graphene-TMDs heterostructures were employed for many other applications, *e.g.* in flexible photodetectors.¹⁰ Nevertheless, the exact physics behind graphene-TMD vdW junctions is still debated^{11–13} and difficult to probe in a direct way. In particular, devices typically include only two contacts, which makes effects on the transport characteristics due to the interface not easy to distinguish from those due to the resistivity of the two-dimensional materials, since typically only the global conductance of the device can be measured. Charge transfer phenomena,¹⁴ strain,¹⁵ and charge trapping in defects,^{16–18} might also play an important role. Furthermore, in the case of field-effect devices, the low density of states in the vicinity of the Dirac point leads to weak screening properties despite the metallic nature of graphene.¹⁹ This implies that a non-trivial response to field effect can be observed, and exploited in device concepts.^{20,21} Gating on graphene-MoS₂ heterostructures has been widely investigated from a numerical²² and experimental^{5,23–25} point of view, and in different stacking configurations. Indeed, the reciprocal electrostatic screening of the junction materials can affect the contact resistance, and it was shown theoretically that MoS₂ can screen the field effect on graphene, or not, depending on the order of the specific stacking sequence.²² Nevertheless, to the best of our knowledge, direct experimental evidence of how the formation of vdW interfaces leads to changes in the transport properties of the individual materials involved in FET devices is still missing.

Results and discussion

The progress of large-scale chemical vapor deposition (CVD) techniques gives the opportunity to investigate vdW interfaces from a different angle. High-quality and large-scale monocrystalline flakes of graphene^{26,27} and TMDs^{28,29} can be reproducibly grown. When this technique is associated with a patterning

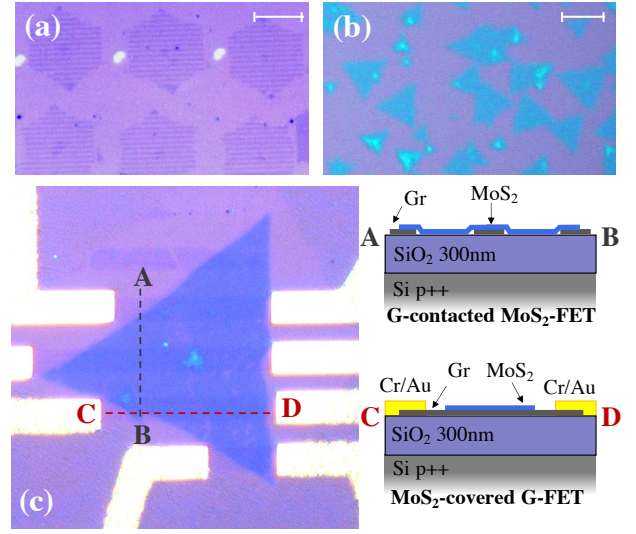


Figure 1: Multi-FET device architecture. (a) Monocrystalline contact stripes obtained by patterning a periodic array of graphene CVD flakes (scale bar is 100 μm). (b) Monocrystalline CVD MoS₂ flakes before transfer onto the SiO₂/Si substrate (scale bar is 50 μm). (c) Optical picture of one of the studied devices implementing a multiple FET structure, as visible in the cross-section sketches: graphene multi-contact MoS₂ FET (AB section) and MoS₂-covered graphene FET (CD section).

of the seed points, predictable flake arrays of chosen sizes can be achieved,³⁰ enabling the fabrication of multiple parallel devices combining different 2D materials. Here, we take advantage of this opportunity to demonstrate a graphene-dichalcogenide architecture where a monocrystalline MoS₂ channel is contacted by a large number of monocrystalline graphene stripes, each of them crossing the whole MoS₂ channel as schematized in Fig. 1. Each stripe can thus act as ohmic contact for a MoS₂ backgated FET (see cross-section AB in Fig. 1), and be simultaneously contacted at its terminations to implement an additional MoS₂-covered graphene FET (cross-section CD in Fig. 1). This structure can so act as a MoS₂ FET and as a set of graphene FETs at the same time, which will be referred to as a *multi-FET* in the following. Such arrangement allows studying the conducting properties for the different components of graphene-MoS₂ systems, highlighting a suppression of the electron-side transconductance

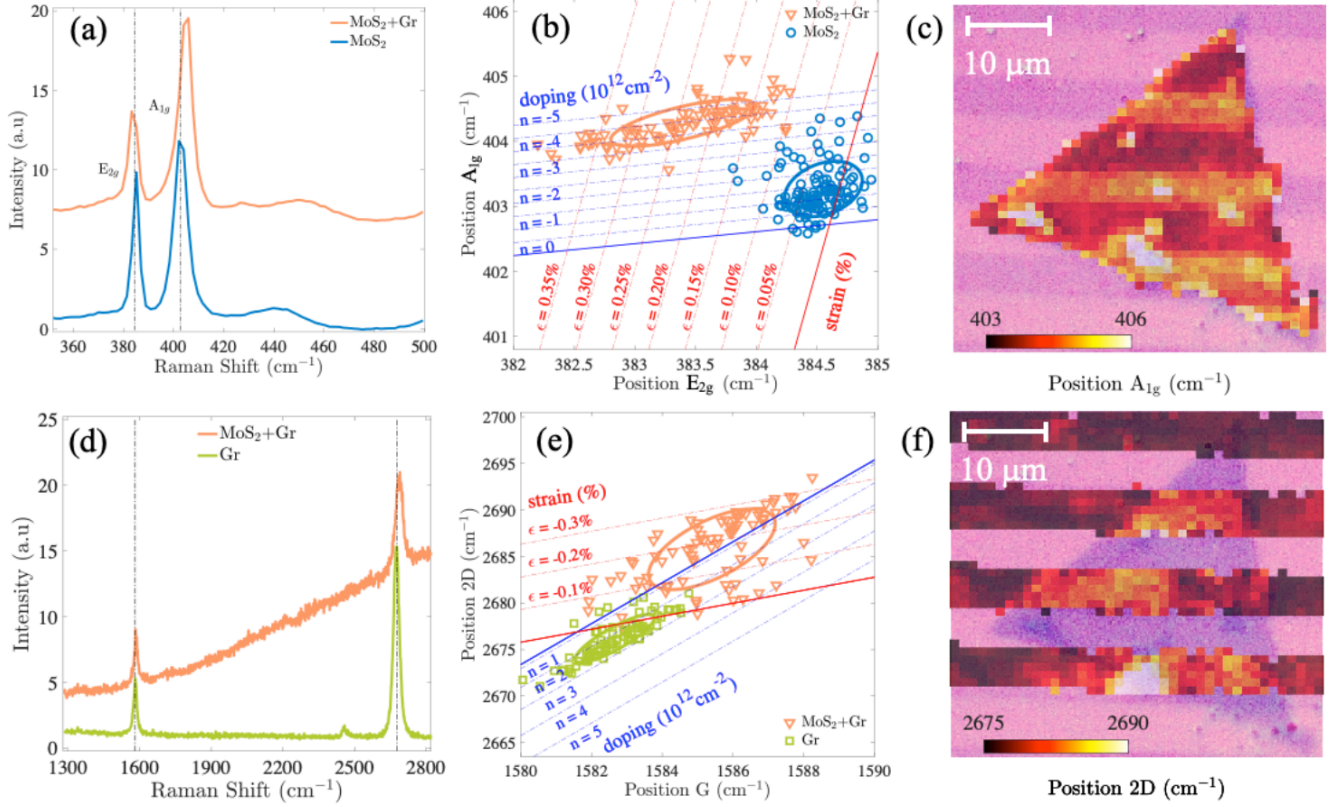


Figure 2: Raman measurements of the MoS₂-graphene structures. (a) MoS₂ Raman spectra after transfer on top of the graphene stripes: both spectra from MoS₂ on top of graphene (orange) and graphene-free MoS₂ (blue) are reported. (b) Correlation plot of the position of A_{1g} as a function of the position of E_{2g}. Zero strain and zero doping line are taken from Ref. 31 (514.5 nm laser excitation). (c) Map of the position of A_{1g}. (d) Raman spectra of graphene after the MoS₂ transfer: both spectra in the presence (orange) and absence (green) of the MoS₂ overlayer are reported. (e) Correlation plot of the position of 2D peak as a function of the position of G peak. Zero strain and zero doping line are taken from Ref. 32 (514.5 nm laser excitation). (f) Map of the position of 2D peak. Correlation plots in panel b and e were obtained from Raman spectra collected as far as possible from the flakes boundaries to avoid spill-over effects from neighboring regions and do not derive from the datasets used in panel c and f.

in MoS₂-covered graphene, in coincidence with the conducting threshold of free MoS₂ in the main device channel. This behavior is apparently at odd with recent predictions for defect-free MoS₂,²² nonetheless it can be understood in terms of a gate-driven trapping by sulfur vacancies which further highlights the non-trivial weak screening properties of graphene.

Both the patterning procedures and the formation of vdW interfaces can significantly perturb the properties of the 2D materials. For this reason, photoluminescence (PL) and Raman spectroscopy were employed to characterize the 2D crystals at relevant device processing steps. In Fig. 2a-c, we report Raman spectra of a typical transferred MoS₂ flake and analyze the influence of the graphene contact stripes. We analyse a MoS₂ flake with a small bilayer island both in regions with and without graphene. The Raman spectra of bilayer MoS₂-graphene heterostructure and bare MoS₂ bilayer are reported in Supporting Information. The characteristic A_{1g} and E_{2g} modes visible in panel (a) exhibit a strong dependence on thickness³³ and their separation $\Delta\omega \simeq 19 \text{ cm}^{-1}$ is in good agreement with the expected monolayer nature of the MoS₂ flake. The shift of the A_{1g} mode in Fig. 2 b-c can be interpreted as caused by the interlayer interaction between MoS₂ and graphene, as reported in Ref. 34. Nevertheless, a recent work³⁵ propose an alternative interpretation in terms of doping and strain, extending the scope of a method which is typically used for bare graphene³² and bare MoS₂.³¹ The following discussion is based on this last interpretation. Starting from strain and doping reference lines reported in Ref. 31, we consider the correlation plot in Fig. 2b, where the position of the A_{1g} peak is plotted against the one of E_{2g} .³¹ Mean Raman shifts of the E_{2g} and A_{1g} peaks in graphene-free regions are $384.5 \pm 0.3 \text{ cm}^{-1}$ and $403.3 \pm 0.4 \text{ cm}^{-1}$, respectively. These values are quite close to the neutrality point, located at the intersection between zero strain and zero doping line ($E_{2g} = 384.6 \pm 0.2 \text{ cm}^{-1}$ and $A_{1g} = 402.7 \pm 0.2 \text{ cm}^{-1}$).³¹ Interestingly, Raman shifts from regions where MoS₂ overlaps graphene ($E_{2g} = 383.4 \pm 0.5 \text{ cm}^{-1}$ and $A_{1g} = 404.3 \pm 0.3 \text{ cm}^{-1}$) indicate a variation in both

tensile strain distribution of $\approx 0.10 - 0.35\%$ and a sizable electron reduction of $(3.0 \pm 1.8) \times 10^{12} \text{ cm}^{-2}$. Thanks to the sensitivity of the A_{1g} peak on doping,³⁶ the spatial doping modulation of MoS₂ due to graphene can be directly appreciated in the map of the A_{1g} position in Fig. 2c. The map is shown in overlay to an optical picture of the flake, to highlight the good correlation between the map patterns and the position of the graphene stripes. Consistent evidences are obtained from graphene Raman data shown in Fig. 2d-f. In panel (d), graphene spectra in the presence/absence of MoS₂ are compared. Both curves show a single sharp Lorentzian-shaped 2D peak, which is a typical signature of monolayer graphene,³⁷ and no D peak, which indicates a negligible density of defects.³⁸ The absence of defects was confirmed for all the fabrication steps (see Supporting Information). We also note that when graphene is covered in MoS₂ (orange curve), a strong baseline appears below the Raman peaks due to the MoS₂ PL signal. As in the case of MoS₂, strain and doping profiles can be derived from the Raman data,³² based on the correlation plot of the 2D and G modes reported in Fig. 2e, where the strain and doping reference lines are taken from Ref. 32, see Supporting Information for additional correlation plots. The positions of the G and 2D peaks in regions free from MoS₂ are $1582.7 \pm 0.9 \text{ cm}^{-1}$ and $2676.2 \pm 2.2 \text{ cm}^{-1}$, respectively, corresponding to a *p*-type doping. Differently, Raman data collected in MoS₂-covered regions ($1585.4 \pm 1.5 \text{ cm}^{-1}$ and $2685.8 \pm 3.7 \text{ cm}^{-1}$ for the G and 2D peaks, respectively) fall on the strain line, thus indicating a neutralization of graphene. The variation of mean peaks positions corresponds to an electron increase of $(2.3 \pm 1.5) \times 10^{12} \text{ cm}^{-2}$ and to a variation of strain nature from tensile to compressive. The spatial modulation of the doping can be seen from the 2D peak position map in panel (f), showing a good correlation with the position of the MoS₂ flake. A modified strain is also observed, turning from slightly tensile to compressive $\approx 0.10 - 0.30\%$. We note that the doping and strain trends observed where MoS₂ and graphene overlap are opposite and thus consistent. We further highlight that, while the

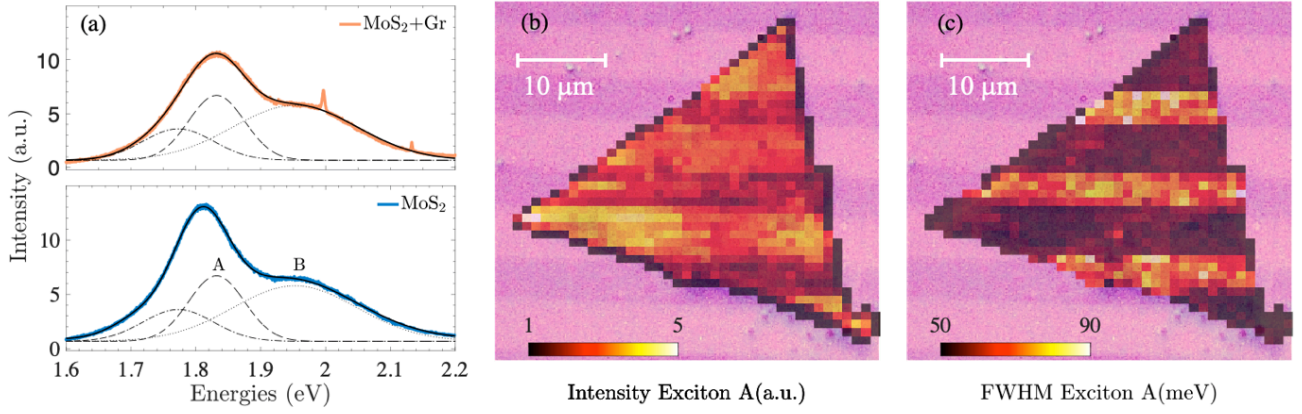


Figure 3: **Photoluminescence measurements of the MoS₂-graphene structures.** (a) PL spectra of MoS₂ both in a region where it overlaps graphene (orange) and in a graphene-free region (blue). Gaussian fits of *A* and *B* excitons are shown in dashed and dot-dashed lines respectively. (b) Map of the position-dependent quenching of the *A* exciton signal. (c) Map of the position-dependent *A* exciton broadening. All maps are shown in overlay to an optical image of the analyzed flake, scalebars in the panels correspond to 10 μm.

discussed analysis of the Raman data indicates an electron transfer from MoS₂ to graphene,³⁵ absolute equilibrium carrier densities are not obvious to quantify. This due to the presence of photo-excited carriers during the Raman measurements, and to the unknown exact calibration of the zero-strain and zero-doping points (standard values from Ref. 32 and 31 were used). The formation of the heterojunction can be further investigated based on the PL spectra of MoS₂, which are reported in Fig. 3a. Three main peaks are highlighted by Gaussian deconvolution. These peaks are attributed to the *A* exciton (1.81 eV), the *B* exciton (1.94 eV) and the trion (1.71 eV).^{39,40} We observe that the presence of graphene modifies the MoS₂ response and the signal of the *A* exciton is quenched when MoS₂ is coupled to graphene (orange curve) with respect to stand-alone MoS₂ (blue curve): indeed, a lowering of the *A* intensity by $\approx 30\%$ and a lineshape broadening from ≈ 66 meV to ≈ 96 meV is retrieved. The spatial modulation of the effect can be directly appreciated from the maps of the intensity and width of the *A* exciton in Fig. 3b and Fig. 3c, respectively. Additional spectroscopic data are reported in the Support-

ing Information.

The graphene stripes form ohmic contacts to the MoS₂ channel and lead, at room temperature and in vacuum conditions ($P < 10^{-5}$ mbar), to highly linear two-wire IV curves over the ± 2 V range. In Fig. 4a, we report the I_{SD} vs. V_{SD} characteristics of a representative MoS₂ FETs, measured as a function of the gate voltage (V_G) in the 0 – 80 V range. The transfer characteristic in Fig. 4b indicates a positive threshold voltage, with a sizable clock-wise hysteresis, as frequently reported in literature for FETs based on 2D materials and nanowires,^{41–45} as well as in Kelvin probe microscopy experiments.⁴⁶ The effect is generally ascribed to the slow dynamics of trap states leading to a time-dependent screening of the field effect of the gate. Trap states may have several origins, including defects at the SiO₂ substrate interface,⁴⁵ adsorbates,⁴⁴ or MoS₂ point defects.⁴³ In our devices, possible sources of traps include interfaces between MoS₂, graphene and SiO₂ (see AFM data in the Supporting Information) as also S vacancies in MoS₂, which are known to occur in quite large densities (typically few 10^{13} cm⁻²) in CVD flakes.^{47,48} The field-effect mobility of MoS₂ car-

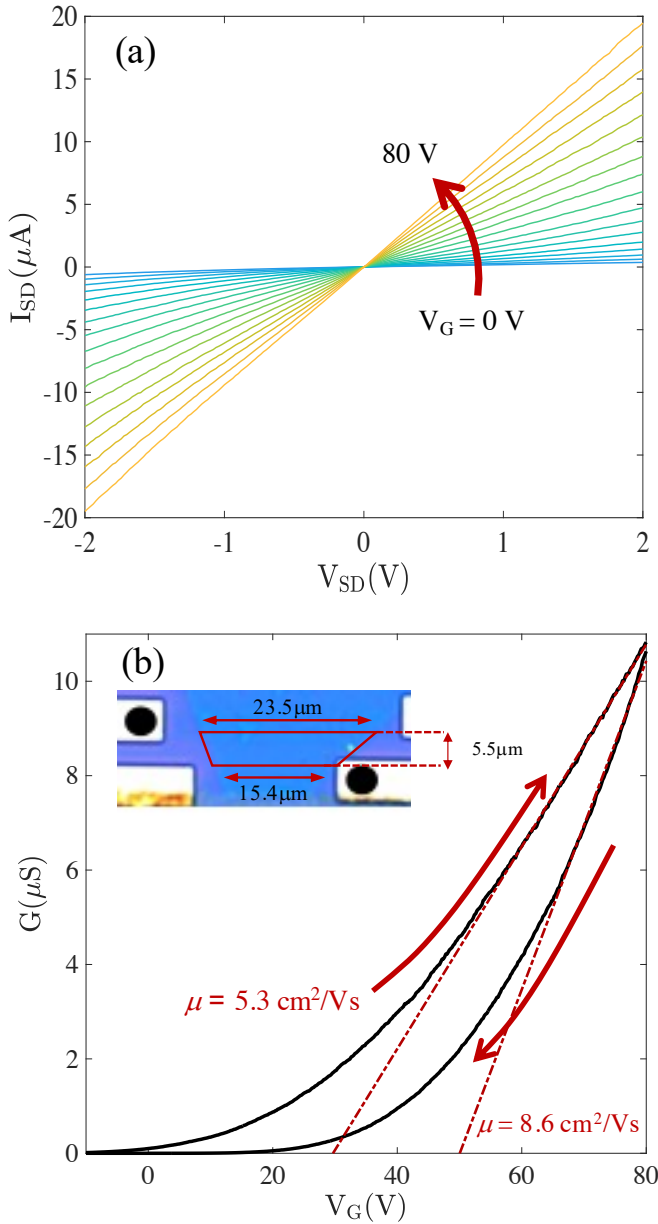


Figure 4: **Transport characteristics of MoS₂.** (a) Room-temperature IV characteristics of the MoS₂ channel as function of the gate voltage V_G in the 0 – 80 V range. (b) Transfer characteristics showing a strong hysteresis, with red arrows indicating the sweep direction. Red dashed lines are the linear fits used to estimate the field-effect mobility for each of the two curves. Inset: an optical image of the measured device, with a sketch of the channel geometry and contacts highlighted by black dots.

rier can be estimated from the transfer characteristic according to

$$\mu = \frac{dG}{dV_G} \frac{L^2}{C_G}, \quad (1)$$

where C_G is the capacitance and the MoS₂ trapezoid channel sketched in the inset of Fig. 4b is approximated as a rectangle with a length $L = 5.5 \pm 0.3 \mu\text{m}$ and width $W = 19.5 \pm 0.5 \mu\text{m}$. Considering both curves in the hysteresis loop, we extract two mobility values $\approx 5.3 \text{ cm}^2/\text{Vs}$ and $\approx 8.6 \text{ cm}^2/\text{Vs}$. Similar analysis on different FETs yielded field-effect mobilities in the range $5.3 - 6.6 \text{ cm}^2/\text{Vs}$. Given that gate hysteresis generally indicates that part of the gate-induced carriers end in charge traps, field-effect measurements are known to overestimate the carrier density induced in the channel and to underestimate mobility.^{42,49} Both the mobility values above should thus be considered as a lower bound to the true room temperature electron mobility in the specific MoS₂ flake. The method also neglects the effect of contact resistances, which may lead to a mobility underestimation but are not expected to have a significant effect in the explored transport regime, based on preliminary four-wire measurement data.

Our multi-FET devices were specifically designed for comparing the MoS₂ transport characteristics with the electron configuration in the graphene stripes, which play here the dual role of the contact in the MoS₂ FET and of the channel in MoS₂-covered graphene FETs. The IVs of all our graphene stripes are found to be highly linear (a representative measurement is reported in Supporting Information) and in Fig. 5 we report the transfer characteristic of various graphene FETs as a function of the V_G , from which we obtain a mobility $\approx 4085 \text{ cm}^2/\text{Vs}$. These measurements are carried out at a fixed $V_{SD} = 0.2 \text{ V}$, as a function of V_G . In the plot sequence (c-g), we compare the conductivity of stripes characterized by a different MoS₂ coverage: conductivity is calculated from the total resistance using the geometrical form factor of the stripe and contact resistances are estimated by comparing the p -side of the gate sweeps; MoS₂ coverage is quantified from the ratio between the area of the MoS₂-graphene and the graphene regions, see optical pictures in Fig. 5a-b. Coverage goes from 0% (MoS₂-free graphene in panel (c)) to 79% (panel (g)). A clear trend is observed in the transfer charac-

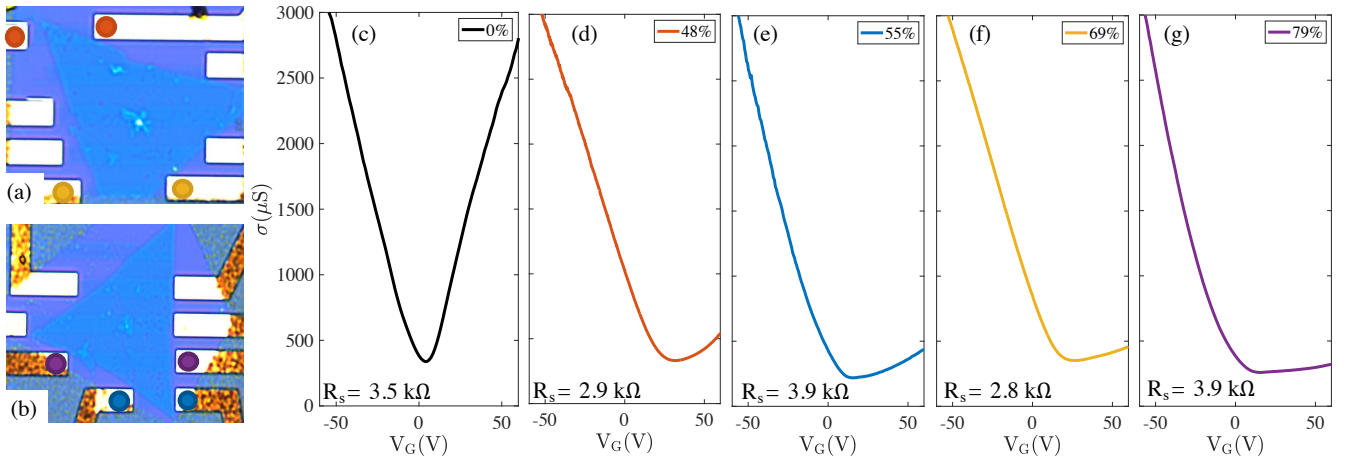


Figure 5: **Effect of the MoS₂ overlayer on electron transport in the graphene contact stripes.** (a-b) Optical images of the two devices used to estimate the effect of different MoS₂ coverage levels on conduction in the graphene stripes. Used contacts are highlighted by colored dots. (c-g) Transfer characteristics of the graphene stripes for different MoS₂ coverages ranging from 0% to 79%. The curve colors match the ones used to highlight the contacts in panels (a) and (b): red 48%, blue 55%, yellow 69%, purple 79%; the black curve corresponds to a reference MoS₂-free graphene stripe (device image not shown).

teristics: curves go from a conventional ambipolar behavior in panel (c) to a limit of strongly quenched n -type conduction for the largest coverage in panel (g). The observation of a quenching of field effect in graphene-TMD heterostructures has been reported in the literature, for both instance in WS₂ and MoS₂-graphene heterostructures, and in graphene functionalized with different materials, such as TiO₂ or organic molecules as well.^{10,17,18,50–52} The important role of MoS₂ on electron transport suppression is clear as no deep suppression is observed in bare graphene stripes on SiO₂ devices.⁵³ On the other hand, the observed behavior is somewhat puzzling since, ideally, MoS₂ should not affect carrier density in graphene when positioned on top of back-gated graphene due to the reciprocal screening in the vdW heterostructure.²²

We ascribe the origin of this apparent discrepancy as due to vacancies in TMDs.^{47,48} This is a reasonable assumption, in fact, as mentioned above another possible source of trap states could be the SiO₂ substrate. Nevertheless, the effect of the SiO₂ substrate is secondary. In fact, the not-covered graphene stripe reported in Fig. 5c has a standard symmetric behavior despite the presence of the SiO₂ substrate.

Moreover, the major contribution to the electron transport suppression from the sulfur vacancies can be deduced from the behavior reported in Fig. 5c-g where a clear trend can be observed: the suppression increases as the MoS₂ coverage increases. Furthermore, it is worth noting that the electrical transport of exfoliated graphene covered by exfoliated MoS₂ usually does not present this suppression of the electron transport.⁵⁴ In order to corroborate our hypothesis, and highlight the effect of sulfur vacancies, we perform Density Functional Theory (DFT) calculations.

Using DFT,⁵⁵ we made an *ab Initio* analysis of the electronic states of graphene-MoS₂⁵⁶ in the presence of sulfur vacancies: these have an energy that falls in the gap⁵⁷ of MoS₂ and are located at a distance of few Angstroms from graphene, so their effect is hard to evaluate without a first-principles approach (see Methods and Supporting Information for further details). Numerical calculations were performed using a density of S-vacancies of $\rho_v \approx 1.8 \times 10^{13} \text{ cm}^{-2}$. In Fig. 6a we report the electronic band structure and projected density of states (DOS) of the graphene-MoS₂ heterostructure for $V_G = 0$: as visible in the plot, the Fermi energy of the system lays in the prox-

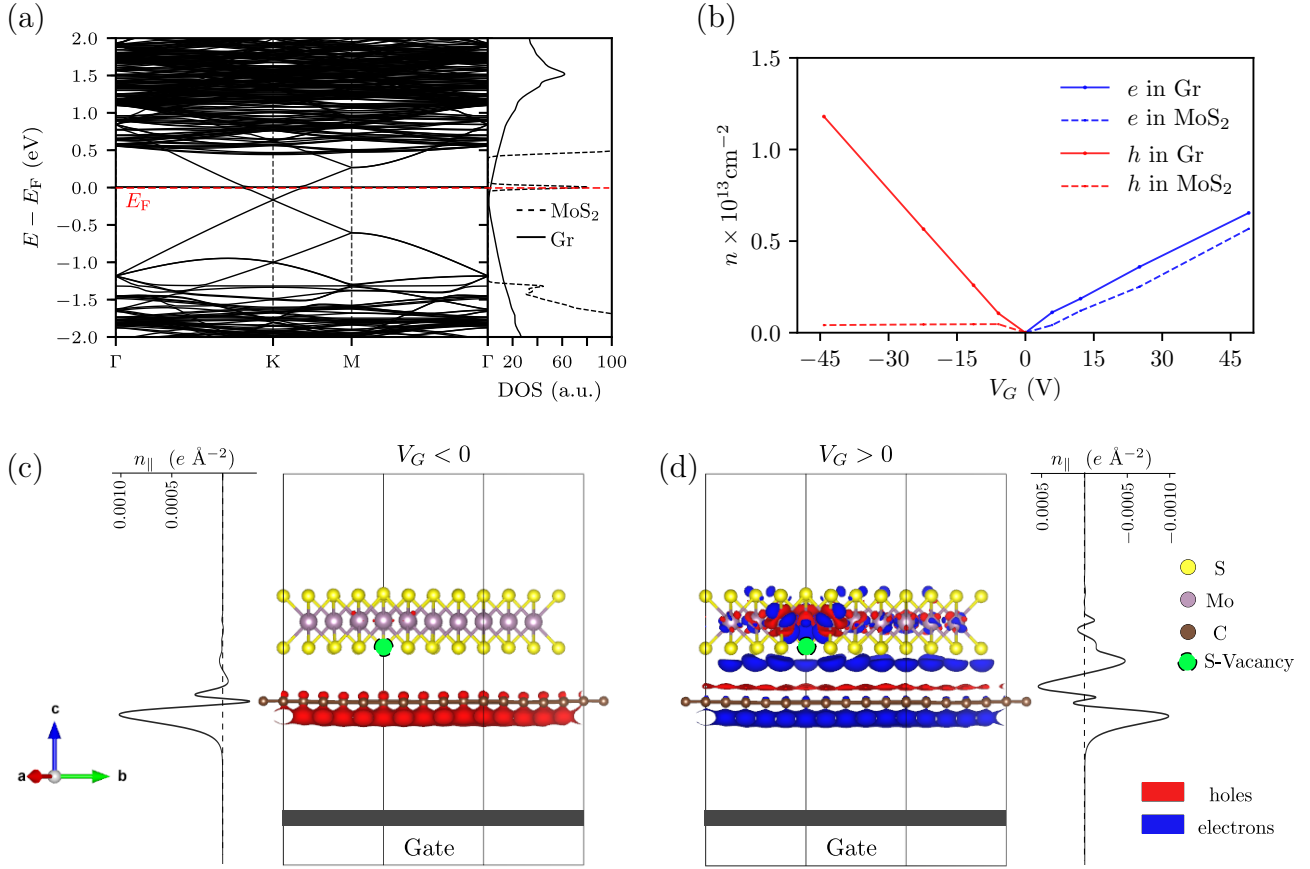


Figure 6: Field-effect response in the presence of S-vacancies. The impact of sulfur vacancies was simulated by removing one S atom from a MoS₂ supercell (density of S-vacancies of $\rho_v \approx 1.8 \times 10^{13} \text{ cm}^{-2}$). (a) Supercell band structure and projected density of states (DOS) of the Graphene-MoS₂ interface ($V_G \approx 23 \text{ V}$ corresponding to a charge induced by field effect $n \approx -6 \times 10^{12} \text{ cm}^{-2}$). The red dashed line indicates the Fermi energy E_F . In the DOS plot, pristine graphene is indicated with a continuous line and the S-vacancy appears as a peak close to the Dirac point. (b) Field-effect induced charge distribution as a function of gate voltage V_G , evaluated as the difference between the gated ($V_G \neq 0$) and ungated case ($V_G = 0$). The solid (dashed) red line indicates the excess holes on the graphene (MoS₂) monolayer, while the solid (dashed) blue line indicates the excess electrons. (c-d) Side view of the gated Graphene-MoS₂ interface. In the two panels, the charge isosurface for $V_G < 0$ (left) and $V_G > 0$ (right) is evaluated as the difference between the charge densities for the gated and ungated limit. The location of the S-vacancy in the supercell is marked by the green ball.

imity of MoS₂ mid-gap states generated by the S-vacancies. This suggests that such states may influence the mobile carrier density induced in the graphene layer by the gate when $V_G \neq 0$. This is confirmed by calculations performed at different values of V_G . As shown in Fig. 6b, even if MoS₂ is placed on top of graphene, it affects the carrier density induced by the gate in the graphene layer. In particular, the n -side of the field-effect response is reduced by $\approx 50\%$; this, combined with the likely increased scattering^{48,58,59} caused by the large DOS close to the Fermi energy, clearly reproduces the behavior reported in Fig. 5. The sulfur vacancies work as charge traps only for positive gate voltages and thus only for electron carriers. The sulfur vacancies generate a midgap state above the neutrality point and scattering due to midgap states reduces the conductivity as described by the formula

$$\sigma = \frac{2e^2}{\pi h} \frac{n_{eff}}{\rho_v} \ln^2(k_F R) \quad (2)$$

where n_{eff} is the effective density of the charge carrier in the graphene sheet ($\approx 50\%$ of the induced doping charge), k_F is the Fermi momentum due to the effective density of the charge carrier n_{eff} , ρ_v is the density of S-vacancies, and $R = 3 \text{ \AA}$ is the average radius of the vacancy.⁴⁸ In Fig. 7, the quantitative estimation of the conductivity is shown. We used a range of ρ_v similar to the one used in the *ab Initio* calculations. We plot the data only for positive gate voltages because the midgap states affect the transport properties only in that sector. In Fig. 6c-d, the atomistic structure and the model of the typical setup for a field-effect measurement are shown. The charge density isosurfaces, together with the planar averaged carrier charge density, give a pictorial view of the different behavior with negative and positive backgate voltages. We point out that our results do not contradict, but rather complement, the conclusion drawn in recent literature:²² calculations also show that no charge transfer is obtained in the case of defect-free MoS₂ since in that limit the TMD cannot support any electron state in the relevant energy range (see Supporting Information). Nonetheless, it is inter-

esting to highlight that, in the presence of vacancies, a TMD overlayer can indeed have an impact on the backgate response of these vdW heterostructures and of devices based on them, extending the range of non-trivial consequences of the weak screening properties of graphene.

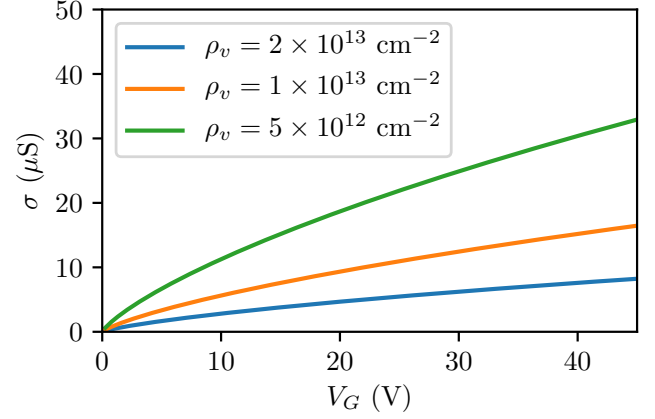


Figure 7: **Quantitative estimate of the conductivity of graphene.** Midgap states associated with sulfur vacancies can suppress mobility in graphene by increasing electron scattering. Conductivity suppression was calculated for three different densities of sulfur vacancies ρ_v , and using the carrier densities reported in Fig. 6.

Conclusions

We have demonstrated a graphene-MoS₂ architecture integrating multiple graphene-contacted MoS₂ FETs and MoS₂-covered graphene FETs and used it to correlate the field-effect characteristics of a MoS₂ monolayer with the conducting properties of graphene used to contact it. Such a study cannot be performed in a conventional FET structure since the individual resistive contributes cannot be discriminated in any obvious and direct way. Our results show that MoS₂ can affect the field-effect conduction of a back-gated graphene monolayer, even when placed on top of the vdW stack, and the suppression of conduction in the graphene stripes is observed over a gate voltage range which is consistent with the conduction threshold of the MoS₂ channel. This behavior is

explained in terms of a filling of sulfur vacancies in the MoS₂, as supported by *ab Initio* calculations. The suppression of the electron transport can be exploited for the development of engineered optoelectronic devices based on van der Waals heterostructures,¹⁰ taking advantage of the low contact resistance of graphene in our multi-FET heterostructure.

Methods

Nanofabrication. The multi-FET fabrication starts from a square array of $\approx 150\text{ }\mu\text{m}$ -wide single-crystal monolayer graphene flakes, with a spacing of $200\text{ }\mu\text{m}$. Arrays are grown on Cu foil *via* CVD³⁰ and then transferred on a p++ Si substrate covered by 300 nm thermal SiO₂ using a delamination procedure and a semi-dry method based on a PMMA vector.²⁶ Before the MoS₂ transfer, the samples were cleaned from PMMA using an overnight immersion in acetone, followed by 2 minutes rinse in isopropanol, 3 minutes in AR 600-71 remover, and finally in deionized water. The next fabrication step was the patterning of graphene into a set of $5\text{ }\mu\text{m}$ -wide and $5\text{ }\mu\text{m}$ -spaced stripes. To this aim, we spun PMMA AR-P679.04 and baked the samples at 120°C for 5 minutes. The stripe patterns were defined *via* electron-beam lithography (EBL) using a *SEM Zeiss Ultraplus* with a Raith lithographic module, an energy of 20 keV and a dose of $300\text{ }\mu\text{C}/\text{cm}^2$. The samples were then developed in AR 600-56 for 2 minutes and a half. Then, graphene was etched by means of reactive ion etching (RIE) using Ar and O₂ (5:80 sccm). Finally, the samples were again cleaned from PMMA with an overnight immersion in acetone and isopropanol rinsing. Single-crystal MoS₂ monolayer flakes with an average size of $\approx 50\text{ }\mu\text{m}$ were grown *via* CVD following Ref. 60 and 61. Single-crystal monolayer MoS₂ flakes were then transferred on the graphene stripes, using a semi-dry method.^{60,61} The transfer process employed for MoS₂ is very similar to the one for graphene except for the delamination step, which was obtained by immersing the sample in a 1 M solution of NaOH rather than by an electrochemical method.⁶⁰

Given the chosen spacing between the stripes, the process typically yields various devices with $4 - 5$ contacts and, since the flakes are triangular, with an uneven coverage of the graphene stripes. A final post-transfer patterning was performed to remove excess material, using a laser writer *Micro Writer ML3* and a S1818 photoresist mask with a 300 nm PMMA interlayer to protect the 2D materials from contamination by the photoresist. We then cleaned the samples with warm acetone (20 minutes) and chloroform for an hour and a half. To complete the devices we defined a set of Cr/Au ($10/50\text{ nm}$) metallic electrodes, *via* EBL, evaporation and lift-off. Using this method, 10 devices were fabricated in two batches and 3 multi-FETs were measured.

Experimental Section The properties of graphene and MoS₂ were monitored by Raman and photoluminescence spectroscopy, using a *Renishaw InVia* spectrometer equipped with a 532 nm laser and $100\times$ objective lens (N.A. 0.85). Laser power was $\approx 1\text{ mW}$ and the typical acquisition time was 4 s .⁶² Transport measurements were performed in a vacuum chamber using source-measure units K4200 and K2614B and a Femto DDPCA-300 current preamplifier.

Numerics. We carried out DFT calculations by using the QUANTUM ESPRESSO (QE),^{63–67} which uses a plane wave basis set. The pseudopotentials were taken from the standard solid-state pseudopotential (SSSP) accuracy library^{68–72} with increased cutoffs of 50 Ry and 400 Ry for the wave functions and the density. The exchange-correlation potential was treated in the GGA, as parametrized by the Perdew-Burke-Ernzerhof (PBE) formula,⁷³ with the van der Waals (vdW)-D2 correction as proposed by Grimme.⁷⁴ For the BZ integrations, we employed a Marzari-Vanderbilt smearing⁷⁵ of 10^{-3} Ry with a Monkhorst-Pack (MP)⁷⁶ \mathbf{k} -point grid with $18\times 18\times 1$ ($24\times 24\times 1$) points for self-consistent calculations of the charge density (density of states). The heterostructure of monolayer MoS₂ on top of monolayer graphene is shown in Fig 6c-d, where a 8×8 MoS₂ supercell is placed on a 10×10 supercell of graphene. The considered heterostructure model contains 391 (392) atoms in the unit cell for the simula-

tion with (without) S-vacancy, corresponding to a density of S-vacancies of $\rho_v \approx 1.8 \times 10^{13} \text{ cm}^{-2}$. We keep the lattice constant of graphene unchanged at $a_0 = 2.46 \text{ \AA}$ ^{55,77} and compressed the lattice constant of MoS₂ by roughly $\approx 2.4\%$: from 3.15 \AA ⁷⁸ to 3.075 \AA . We considered a supercell with about 18 \AA of vacuum along the \hat{c} -direction between periodic images. We optimize the geometrical structures by relaxing only the atomic positions until the components of all the forces on the ions are less than 10^{-3} Ry/Bohr , while we keep fixed the lattice parameters.

In Fig. 6c-d, a model of the typical setup for a field-effect measurement is shown. The Graphene-MoS₂ is placed in front of a metal gate. The layers are then charged with the same amount of opposite charge, leading to a finite electric field in the region between the heterostructure and the gate. In order to avoid spurious and artificial electric field between the different slabs of the repeated unit cell, an electric field generated by a dipole plate of opposite charge has been included next to the gate. Furthermore, to avoid the direct interaction between the charge-density of the system and the gate, a potential barrier has been included.^{66,67} In order to mimic the experimental values, in Fig. 6b, we rescaled the values of V_G considering that in the real experiment there is a 300 nm thick layer of SiO₂ between the metal gate and the Graphene-MoS₂ interface. We use the VESTA⁷⁹ code to visualize the geometrical structure, the isosurfaces, and to produce the plots in Fig. 6. To obtain information on the charge transfer between the two moieties (Graphene-MoS₂) we performed a topological analysis of the electron density by means of the Bader procedure^{80–83} as implemented in CRITIC2.^{84,85}

Acknowledgement G.M. thanks G. Grosso for useful discussions. G.C. thanks L. Martini for useful discussions. SR and AT acknowledge the support of the Italian Ministry of Research through the PRIN projects “Quantum 2D” and “Monstre 2D”, respectively. G.M. acknowledges the “IT center” of the University of Pisa, the HPC center (Franklin) of the IIT

of Genova, and the allocation of computer resources from CINECA, through the “ISCRA C” projects “HP10C9JF51”, “HP10CI1LTC”, “HP10CY46PW”, “HP10CMQ8ZK”. The research leading to these results has received funding from the European Union’s Horizon 2020 research and innovation program under grant agreement no. 881603-Graphene Core3.

Supporting Information Available

Additional Raman data, additional photoluminescence data, atomic force microscopy measurement, additional DFT results.

References

1. Geim, A. K.; Grigorieva, I. V. van der Waals Heterostructures. *Nature* **2013**, *499*, 419–425.
2. Kim, C.; Moon, I.; Lee, D.; Choi, M. S.; Ahmed, F.; Nam, S.; Cho, Y.; Shin, H.-J.; Park, S.; Yoo, W. J. Fermi Level Pinning at Electrical Metal Contacts of Monolayer Molybdenum Dichalcogenides. *ACS Nano* **2017**, *11*, 1588–1596.
3. Sotthewes, K.; van Bremen, R.; Dollekamp, E.; Boulogne, T.; Nowakowski, K.; Kas, D.; Zandvliet, H. J. W.; Bampoulis, P. Universal Fermi-Level Pinning in Transition-Metal Dichalcogenides. *J. Phys. Chem. C* **2019**, *123*, 5411–5420.
4. Das, S.; Chen, H.-Y.; Penumatcha, A. V.; Appenzeller, J. High Performance Multilayer MoS₂ Transistors with Scandium Contacts. *Nano Lett.* **2013**, *13*, 100–105.
5. Liu, Y.; Wu, H.; Cheng, H.-C.; Yang, S.; Zhu, E.; He, Q.; Ding, M.; Li, D.; Guo, J.; Weiss, N. O.; Huang, Y.; Duan, X. Toward Barrier Free Contact to Molybdenum Disulfide Using Graphene Electrodes. *Nano Lett.* **2015**, *15*, 3030–3034.

6. Chuang, H.-J.; Tan, X.; Ghimire, N. J.; Perera, M. M.; Chamlagain, B.; Cheng, M. M.-C.; Yan, J.; Mandrus, D.; Tománek, D.; Zhou, Z. High Mobility WSe₂ *p*- and *n*-Type Field-Effect Transistors Contacted by Highly Doped Graphene for Low-Resistance Contacts. *Nano Lett.* **2014**, *14*, 3594–3601.
7. L., W.; I., M.; Y., H. P.; Q., G.; Y., G.; H., T.; T., T.; K., W.; M., C. L.; A., M. D.; J., G.; P., K.; J., H.; L., S. K.; R., D. C. One-Dimensional Electrical Contact to a Two-Dimensional Material. *Science* **2013**, *342*, 614–617.
8. Matsuda, Y.; Deng, W.-Q.; Goddard, W. A. Contact Resistance for 'End-Contacted' Metal-Graphene and Metal-Nanotube Interfaces from Quantum Mechanics. *J. Phys. Chem. C* **2010**, *114*, 17845–17850.
9. Yu, H.; Gupta, S.; Kutana, A.; Yakobson, B. I. Dimensionality-Reduced Fermi Level Pinning in Coplanar 2D Heterojunctions. *J. Phys. Chem. Lett.* **2021**, *12*, 4299–4305.
10. De Fazio, D.; Goykhman, I.; Yoon, D.; Bruna, M.; Eiden, A.; Milana, S.; Sassi, U.; Barbone, M.; Dumcenco, D.; Marinov, K.; Kis, A.; Ferrari, A. C. High Responsivity, Large-Area Graphene/MoS₂ Flexible Photodetectors. *ACS Nano* **2016**, *10*, 8252–8262.
11. Yu, W. J.; Li, Z.; Zhou, H.; Chen, Y.; Wang, Y.; Huang, Y.; Duan, X. Vertically Stacked Multi-Heterostructures of Layered Materials for Logic Transistors and Complementary Inverters. *Nat. Mater.* **2013**, *12*, 246–252.
12. Kwak, J. Y.; Hwang, J.; Calderon, B.; Alsalman, H.; Munoz, N.; Schutter, B.; Spencer, M. G. Electrical Characteristics of Multilayer MoS₂ FET's with MoS₂/Graphene Heterojunction Contacts. *Nano Lett.* **2014**, *14*, 4511–4516.
13. Tian, H.; Tan, Z.; Wu, C.; Wang, X.; Mohammad, M. A.; Xie, D.; Yang, Y.; Wang, J.; Li, L.-J.; Xu, J.; Ren, T.-L. Novel Field-Effect Schottky Barrier Transistors Based on Graphene-MoS₂ Heterojunctions. *Sci. Rep.* **2014**, *4*, 5951.
14. Dappe, Y. J.; Almadori, Y.; Dau, M. T.; Vergnaud, C.; Jamet, M.; Paillet, C.; Journot, T.; Hyot, B.; Pochet, P.; Grévin, B. Charge Transfers and Charged Defects in WSe₂/Graphene-SiC Interfaces. *Nanotechnology* **2020**, *31*, 255709.
15. Liu, X.; Li, Z. Electric Field and Strain Effect on Graphene-MoS₂ Hybrid Structure: *ab Initio* Calculations. *J. Phys. Chem. Lett.* **2015**, *6*, 3269–3275.
16. Han, Y.; Wu, Z.; Xu, S.; Chen, X.; Wang, L.; Wang, Y.; Xiong, W.; Han, T.; Ye, W.; Lin, J.; Cai, Y.; Ho, K. M.; He, Y.; Su, D.; Wang, N. Probing Defect-Induced Midgap States in MoS₂ through Graphene-MoS₂ Heterostructures. *Adv. Mater. Interfaces* **2015**, *2*, 1500064.
17. Piccinini, G.; Forti, S.; Martini, L.; Pezzini, S.; Miseikis, V.; Starke, U.; Fabbri, F.; Coletti, C. Deterministic Direct Growth of WS₂ on Graphene Arrays. *2D Mater.* **2019**, *7*, 014002.
18. Avsar, A.; Tan, J. Y.; Taychatanapat, T.; Balakrishnan, J.; Koon, G. K. W.; Yeo, Y.; Lahiri, J.; Carvalho, A.; Rodin, A. S.; O'Farrell, E. C. T.; Eda, G.; Castro Neto, A. H.; Özyilmaz, B. Spin-Orbit Proximity Effect in Graphene. *Nat. Commun.* **2014**, *5*, 4875.
19. Li, L. H.; Tian, T.; Cai, Q.; Shih, C.-J.; Santos, E. J. G. Asymmetric Electric Field Screening in van der Waals Heterostructures. *Nat. Commun.* **2018**, *9*, 1271.
20. Zhu, X.; Li, D.; Liang, X.; Lu, W. D. Ionic Modulation and Ionic Coupling Effects in MoS₂ Devices for Neuromorphic Computing. *Nat. Mater.* **2019**, *18*, 141–148.

21. Krishnaprasad, A.; Choudhary, N.; Das, S.; Dev, D.; Kalita, H.; Chung, H.-S.; Aina, O.; Jung, Y.; Roy, T. Electronic Synapses with Near-Linear Weight Update Using MoS₂/Graphene Memristors. *Appl. Phys. Lett.* **2019**, *115*, 103104.
22. Stradi, D.; Papior, N. R.; Hansen, O.; Brandbyge, M. Field Effect in Graphene-Based van der Waals Heterostructures: Stacking Sequence Matters. *Nano Lett.* **2017**, *17*, 2660–2666.
23. Cui, X.; Lee, G.-H.; Kim, Y. D.; Arefe, G.; Huang, P. Y.; Lee, C.-H.; Chenet, D. A.; Zhang, X.; Wang, L.; Ye, F.; Pizzocchero, F.; Jessen, B. S.; Watanabe, K.; Taniguchi, T.; Muller, D. A.; Low, T.; Kim, P.; Hone, J. Multi-Terminal Transport Measurements of MoS₂ Using a van der Waals Heterostructure Device Platform. *Nat. Nanotechnol.* **2015**, *10*, 534–540.
24. Lee, G.-H.; Cui, X.; Kim, Y. D.; Arefe, G.; Zhang, X.; Lee, C.-H.; Ye, F.; Watanabe, K.; Taniguchi, T.; Kim, P.; Hone, J. Highly Stable, Dual-Gated MoS₂ Transistors Encapsulated by Hexagonal Boron Nitride with Gate-Controllable Contact, Resistance, and Threshold Voltage. *ACS Nano* **2015**, *9*, 7019–7026.
25. Bertolazzi, S.; Krasnozhan, D.; Kis, A. Nonvolatile Memory Cells Based on MoS₂/Graphene Heterostructures. *ACS Nano* **2013**, *7*, 3246–3252.
26. Giambra, M. A.; Mišeikis, V.; Pezzini, S.; Marconi, S.; Montanaro, A.; Fabbri, F.; Sorianello, V.; Ferrari, A. C.; Coletti, C.; Romagnoli, M. Wafer-Scale Integration of Graphene-Based Photonic Devices. *ACS Nano* **2021**, *15*, 3171–3187.
27. Wang, M.; Luo, D.; Wang, B.; Ruoff, R. S. Synthesis of Large-Area Single-Crystal Graphene. *Trends Chem.* **2021**, *3*, 15–33.
28. Schram, T.; Smets, Q.; Groven, B.; Heyne, M. H.; Kunnen, E.; Thiam, A.; Devriendt, K.; Delabie, A.; Lin, D.; Lux, M.; Chiappe, D.; Asselberghs, I.; Brus, S.; Huyghebaert, C.; Sayan, S.; Juncker, A.; Caymax, M.; Radu, I. P. WS₂ Transistors on 300 mm Wafers with BEOL Compatibility. In *2017 47th European Solid-State Device Research Conference (ESSDERC)* **2017**, Leuven, Belgium, Sept 11–14, 2017; IEEE, 2017; pp 212–215. DOI: 10.1109/ESSDERC.2017.8066629 .
29. Cun, H.; Macha, M.; Kim, H.; Liu, K.; Zhao, Y.; LaGrange, T.; Kis, A.; Radenovic, A. Wafer-Scale MOCVD Growth of Monolayer MoS₂ on Sapphire and SiO₂. *Nano Res.* **2019**, *12*, 2646–2652.
30. Miseikis, V.; Bianco, F.; David, J.; Gemmi, M.; Pellegrini, V.; Romagnoli, M.; Coletti, C. Deterministic Patterned Growth of High-Mobility Large-Crystal Graphene: a Path towards Wafer Scale Integration. *2D Mater.* **2017**, *4*, 021004.
31. Michail, A.; Delikoukos, N.; Parthenios, J.; Galiotis, C.; Papagelis, K. Optical Detection of Strain and Doping Inhomogeneities in Single Layer MoS₂. *Appl. Phys. Lett.* **2016**, *108*, 173102.
32. Lee, J. E.; Ahn, G.; Shim, J.; Lee, Y. S.; Ryu, S. Optical Separation of Mechanical Strain from Charge Doping in Graphene. *Nat. Commun.* **2012**, *3*, 1024.
33. Lee, C.; Yan, H.; Brus, L. E.; Heinz, T. F.; Hone, J.; Ryu, S. Anomalous Lattice Vibrations of Single- and Few-Layer MoS₂. *ACS Nano* **2010**, *4*, 2695–2700.
34. Zhou, K.-G.; Withers, F.; Cao, Y.; Hu, S.; Yu, G.; Casiraghi, C. Raman Modes of MoS₂ Used as Fingerprint of van der Waals Interactions in 2-D Crystal-Based Heterostructures. *ACS Nano* **2014**, *8*, 9914–9924.
35. Rao, R.; Islam, A. E.; Singh, S.; Berry, R.; Kawakami, R. K.; Maruyama, B.; Katoch, J. Spectroscopic Evaluation of Charge-Transfer Doping and Strain in Graphene/MoS₂ Heterostructures. *Phys. Rev. B* **2019**, *99*, 195401–.

36. Chakraborty, B.; Bera, A.; Muthu, D. V. S.; Bhowmick, S.; Waghmare, U. V.; Sood, A. K. Symmetry-Dependent Phonon Renormalization in Monolayer MoS₂ Transistor. *Phys. Rev. B* **2012**, *85*, 161403.
37. Ferrari, A. C.; Meyer, J. C.; Scardaci, V.; Casiraghi, C.; Lazzeri, M.; Mauri, F.; Piscanec, S.; Jiang, D.; Novoselov, K. S.; Roth, S.; Geim, A. K. Raman Spectrum of Graphene and Graphene Layers. *Phys. Rev. Lett.* **2006**, *97*, 187401.
38. Cançado, L. G.; Jorio, A.; Ferreira, E. H. M.; Stavale, F.; Achete, C. A.; Capaz, R. B.; Moutinho, M. V. O.; Lombardo, A.; Kulmala, T. S.; Ferrari, A. C. Quantifying Defects in Graphene *via* Raman Spectroscopy at Different Excitation Energies. *Nano Lett.* **2011**, *11*, 3190–3196.
39. Mouri, S.; Miyauchi, Y.; Matsuda, K. Tunable Photoluminescence of Monolayer MoS₂ *via* Chemical Doping. *Nano Lett.* **2013**, *13*, 5944–5948.
40. Splendiani, A.; Sun, L.; Zhang, Y.; Li, T.; Kim, J.; Chim, C.-Y.; Galli, G.; Wang, F. Emerging Photoluminescence in Monolayer MoS₂. *Nano Lett.* **2010**, *10*, 1271–1275.
41. Mitta, S. B.; Choi, M. S.; Nipane, A.; Ali, F.; Kim, C.; Teherani, J. T.; Hone, J.; Yoo, W. J. Electrical Characterization of 2D Materials-Based Field-Effect Transistors. *2D Mater.* **2020**, *8*, 012002.
42. Roddaro, S.; Ercolani, D.; Safeen, M. A.; Suomalainen, S.; Rossella, F.; Giazotto, F.; Sorba, L.; Beltram, F. Giant Thermovoltage in Single InAs Nanowire Field-Effect Transistors. *Nano Lett.* **2013**, *13*, 3638–3642.
43. Bartolomeo, A. D.; Genovese, L.; Giubileo, F.; Iemmo, L.; Luongo, G.; Foller, T.; Schleberger, M. Hysteresis in the Transfer Characteristics of MoS₂ Transistors. *2D Mater.* **2017**, *5*, 015014.
44. Late, D. J.; Liu, B.; Matte, H. S. S. R.; David, V. P.; Rao, C. N. R. Hysteresis in Single-Layer MoS₂ Field Effect Transistors. *ACS Nano* **2012**, *6*, 5635–5641.
45. Vu, Q. A.; Fan, S.; Lee, S. H.; Joo, M.-K.; Yu, W. J.; Lee, Y. H. Near-Zero Hysteresis and Near-Ideal Subthreshold Swing in h-BN Encapsulated Single-Layer MoS₂ Field-Effect Transistors. *2D Mater.* **2018**, *5*, 031001.
46. Wang, Y.; Li, D.; Lai, X.; Liu, B.; Chen, Y.; Wang, F.; Wang, R.; Zhang, L. Direct Observation of the Hysteretic Fermi Level Modulation in Monolayer MoS₂ Field Effect Transistors. *Curr. Appl. Phys.* **2020**, *20*, 298–303.
47. Hong, J.; Hu, Z.; Probert, M.; Li, K.; Lv, D.; Yang, X.; Gu, L.; Mao, N.; Feng, Q.; Xie, L.; Zhang, J.; Wu, D.; Zhang, Z.; Jin, C.; Ji, W.; Zhang, X.; Yuan, J.; Zhang, Z. Exploring Atomic Defects in Molybdenum Disulphide Monolayers. *Nat. Commun.* **2015**, *6*, 6293.
48. Qiu, H.; Xu, T.; Wang, Z.; Ren, W.; Nan, H.; Ni, Z.; Chen, Q.; Yuan, S.; Miao, F.; Song, F.; Long, G.; Shi, Y.; Sun, L.; Wang, J.; Wang, X. Hopping Transport through Defect-Induced Localized States in Molybdenum Disulphide. *Nat. Commun.* **2013**, *4*, 2642.
49. Pitanti, A.; Roddaro, S.; Vitiello, M. S.; Tredicucci, A. Contacts Shielding in Nanowire Field Effect Transistors. *J. Appl. Phys.* **2012**, *111*, 064301.
50. Yan, Z.; Yao, J.; Sun, Z.; Zhu, Y.; Tour, J. M. Controlled Ambipolar-to-Unipolar Conversion in Graphene Field-Effect Transistors through Surface Coating with Poly(ethylene Imine)/Poly(ethylene Glycol) Films. *Small* **2012**, *8*, 59–62.
51. Li, H.; Zhang, Q.; Liu, C.; Xu, S.; Gao, P. Ambipolar to Unipolar Conversion in Graphene Field-Effect Transistors. *ACS Nano* **2011**, *5*, 3198–3203.

52. Kim, M.; Safron, N. S.; Huang, C.; Arnold, M. S.; Gopalan, P. Light-Driven Reversible Modulation of Doping in Graphene. *Nano Lett.* **2012**, *12*, 182–187.
53. Tyagi, A.; Mišeikis, V.; Martini, L.; Forti, S.; Mishra, N.; Gebeyehu, Z. M.; Giambra, M. A.; Zribi, J.; Frégnaux, M.; Aureau, D.; Romagnoli, M.; Beltram, F.; Coletti, C. Ultra-Clean High-Mobility Graphene on Technologically Relevant Substrates. **2021**, 2109.00308. arXiv. <https://arxiv.org/abs/2109.00308> (accessed 12 14, 2021).
54. Moriya, R.; Yamaguchi, T.; Inoue, Y.; Sata, Y.; Morikawa, S.; Masubuchi, S.; Machida, T. Influence of the Density of States of Graphene on the Transport Properties of Graphene/MoS₂/Metal Vertical Field-Effect Transistors. *Appl. Phys. Lett.* **2015**, *106*, 223103.
55. Grosso, G.; Parravicini, G. P. *Solid State Physics*, 2nd ed.; Academic Press: London, 2014.
56. Giuliani, G.; Vignale, G. *Quantum Theory of the Electron Liquid*; Cambridge University Press: Cambridge, 2005.
57. Bussolotti, F.; Yang, J.; Kawai, H.; Wong, C. P. Y.; Goh, K. E. J. Impact of S-Vacancies on the Charge Injection Barrier at the Electrical Contact with the MoS₂ Monolayer. *ACS Nano* **2021**, *15*, 2686–2697.
58. Das Sarma, S.; Adam, S.; Hwang, E. H.; Rossi, E. Electronic Transport in Two-Dimensional Graphene. *Rev. Mod. Phys.* **2011**, *83*, 407–470.
59. Stauber, T.; Peres, N. M. R.; Guinea, F. Electronic Transport in Graphene: A Semiclassical Approach Including Midgap States. *Phys. Rev. B* **2007**, *76*, 205423–.
60. Conti, S.; Pimpolari, L.; Calabrese, G.; Worsley, R.; Majee, S.; Polyushkin, D. K.; Paur, M.; Pace, S.; Keum, D. H.; Fabbri, F.; Iannaccone, G.; Macucci, M.; Coletti, C.; Mueller, T.; Casiraghi, C.; Fiori, G. Low-Voltage 2D Materials-Based Printed Field-Effect Transistors for Integrated Digital and Analog Electronics on Paper. *Nat. Commun.* **2020**, *11*, 3566.
61. Kim, H.; Han, G. H.; Yun, S. J.; Zhao, J.; Keum, D. H.; Jeong, H. Y.; Ly, T. H.; Jin, Y.; Park, J.-H.; Moon, B. H.; Kim, S.-W.; Lee, Y. H. Role of Alkali Metal Promoter in Enhancing Lateral Growth of Monolayer Transition Metal Dichalcogenides. *Nanotechnology* **2017**, *28*, 36LT01.
62. Pace, S.; Ferrera, M.; Convertino, D.; Piccinini, G.; Magnozzi, M.; Mishra, N.; Forti, S.; Bisio, F.; Canepa, M.; Fabbri, F.; Coletti, C. Thermal Stability of Monolayer WS₂ in BEOL Conditions. *JPhys Mater.* **2021**, *4*, 024002.
63. Giannozzi, P.; Baroni, S.; Bonini, N.; Calandra, M.; Car, R.; Cavazzoni, C.; Ceresoli, D.; Chiarotti, G. L.; Cococcioni, M.; Dabo, I.; Dal Corso, A.; de Gironcoli, S.; Fabris, S.; Fratesi, G.; Gebauer, R.; Gerstmann, U.; Gougoussis, C.; Kokalj, A.; Lazzeri, M.; Martin-Samos, L. *et al.* QUANTUM ESPRESSO: A Modular and Open-Source Software Project for Quantum Simulations of Materials. *J. Phys.: Condens. Matter* **2009**, *21*, 395502.
64. Giannozzi, P.; Andreussi, O.; Brumme, T.; Bunau, O.; Buongiorno Nardelli, M.; Calandra, M.; Car, R.; Cavazzoni, C.; Ceresoli, D.; Cococcioni, M.; Colonna, N.; Carnimeo, I.; Dal Corso, A.; de Gironcoli, S.; Delugas, P.; DiStasio, R. A.; Ferretti, A.; Floris, A.; Fratesi, G.; Fugallo, G. *et al.* Advanced Capabilities for Materials Modelling with QUANTUM ESPRESSO. *J. Phys.: Condens. Matter* **2017**, *29*, 465901.
65. Giannozzi, P.; Baseggio, O.; Bonfà, P.; Brunato, D.; Car, R.; Carnimeo, I.; Cavazzoni, C.; de Gironcoli, S.; Delugas, P.; Ferretti, A.; Marzari, N.;

- Timrov, I.; Urru, A.; Baroni, S. QUANTUM ESPRESSO toward the Exascale. *J. Chem. Phys.* **2020**, *152*, 154105.
66. Brumme, T.; Calandra, M.; Mauri, F. Electrochemical Doping of Few-Layer ZrNCl from First Principles: Electronic and Structural Properties in Field-Effect Configuration. *Phys. Rev. B* **2014**, *89*, 245406.
 67. Brumme, T.; Calandra, M.; Mauri, F. First-Principles Theory of Field-Effect Doping in Transition-Metal Dichalcogenides: Structural Properties, Electronic Structure, Hall Coefficient, and Electrical Conductivity. *Phys. Rev. B* **2015**, *91*, 155436.
 68. Prandini, G.; Marrazzo, A.; Castelli, I. E.; Mounet, N.; Marzari, N. Precision and Efficiency in Solid-State Pseudopotential Calculations. *Npj Comput. Mater.* **2018**, *4*, 72.
 69. Lejaeghere, K.; Bihlmayer, G.; Björkman, T.; Blaha, P.; Blügel, S.; Blum, V.; Caliste, D.; Castelli, I. E.; Clark, S. J.; Dal Corso, A.; de Gironcoli, S.; Deutsch, T.; Dewhurst, J. K.; Di Marco, I.; Draxl, C.; Dułak, M.; Eriksson, O.; Flores-Livas, J.; Garrity, K. F.; Genovese, L. *et al.* Reproducibility in Density Functional Theory Calculations of Solids. *Science* **2016**, *351*, aad3000.
 70. Schlipf, M.; Gygi, F. Optimization Algorithm for the Generation of ONCV Pseudopotentials. *Comput. Phys. Commun.* **2015**, *196*, 36–44.
 71. Dal Corso, A. Pseudopotentials Periodic Table: From H to Pu. *Comput. Mater. Sci.* **2014**, *95*, 337–350.
 72. Garrity, K. F.; Bennett, J. W.; Rabe, K. M.; Vanderbilt, D. Pseudopotentials for High-Throughput DFT Calculations. *Comput. Mater. Sci.* **2014**, *81*, 446–452.
 73. Perdew, J. P.; Burke, K.; Ernzerhof, M. Generalized Gradient Approximation Made Simple. *Phys. Rev. Lett.* **1996**, *77*, 3865–3868.
 74. Grimme, S. Semiempirical GGA-Type Density Functional Constructed with a Long-Range Dispersion Correction. *J. Comput. Chem.* **2006**, *27*, 1787–1799.
 75. Marzari, N.; Vanderbilt, D.; De Vita, A.; Payne, M. C. Thermal Contraction and Disordering of the Al(110) Surface. *Phys. Rev. Lett.* **1999**, *82*, 3296–3299.
 76. Monkhorst, H. J.; Pack, J. D. Special Points for Brillouin-Zone Integrations. *Phys. Rev. B* **1976**, *13*, 5188–5192.
 77. Colle, R.; Menichetti, G.; Grosso, G. Graphene on Clean (0001)-Quartz: Numerical Determination of a Minimum Energy Path from Metal to Semiconductor. *Phys. Status Solidi B* **2016**, *253*, 1799–1807.
 78. Wakabayashi, N.; Smith, H. G.; Nicklow, R. M. Lattice Dynamics of Hexagonal MoS₂ Studied by Neutron Scattering. *Phys. Rev. B* **1975**, *12*, 659–663.
 79. Momma, K.; Izumi, F. VESTA3 for Three-Dimensional Visualization of Crystal, Volumetric and Morphology Data. *J. Appl. Crystallogr.* **2011**, *44*, 1272–1276.
 80. Bader, R. *Atoms in Molecules: A Quantum Theory*; International Series of Monographs on Chemistry; Clarendon Press: Oxford, 1990.
 81. Gatti, C. Chemical Bonding in Crystals: New Directions. *Z. Kristallogr. Cryst. Mater.* **2005**, *220*, 399–457.
 82. Menichetti, G.; Colle, R.; Gatti, C.; Grosso, G. Heterointerface Electronic States and Charge Transport of Crystalline N,N'-1H,1H'-Perfluorobutyl Dicyanoperylene Diimide in Field-Effect Transistor Configuration. *J. Phys. Chem. C* **2016**, *120*, 12083–12091.
 83. Menichetti, G.; Colle, R.; Grosso, G. Strain Modulation of Band Offsets at

the PCBM/P3HT Heterointerface. *J. Phys. Chem. C* **2017**, *121*, 13707–13716.

84. Otero-de-la Roza, A.; Johnson, E. R.; Luaña, V. Critic2: A Program for Real-Space Analysis of Quantum Chemical Interactions in Solids. *Comput. Phys. Commun.* **2014**, *185*, 1007–1018.
85. Otero-de-la Roza, A.; Blanco, M. A.; Pendás, A. M.; Luaña, V. Critic: A New Program for the Topological Analysis of Solid-State Electron Densities. *Comput. Phys. Commun.* **2009**, *180*, 157–166.